POLARIMETRIC BRIGHTNESS TEMPERATURES OF SEA SURFACES MEASURED WITH AIRCRAFT K- AND Ka-BAND RADIOMETERS

Simon H. Yueh, William J. Wilson, Fuk K. Li, Son V. Nghiem
and William B. Ricketts

Jet Propulsion Laboratory
California Institute of Technology
4800 Oak Grove Drive
Pasadena, CA 91109
Tel: (818) 354-3012, Fax: (818) 393-5285

Submitted to IEEE Trans. Geosci. Remote Sensing on January 16, 1995

Author -
"Wave number" is shown in my dictionary as 2 words. (In this document, it appears as one.)

Author -
I'm used to seeing "kelvin" as the unit of measure, rather than "Kelvin" (lowercase "k"). Also, when several or a few are spoken of, I'm used to seeing it in the plural (e.g., "a few kelvins" or "several kelvins").

Abstract

Dual-frequency (19 and 37 GHz), multi-incidence measurements of the Stokes parameters of sea surface microwave emission are reported in this paper. A series of aircraft polarimetric radiometer flights were carried out over the National Data Buoy Center (NDBC) moored buoys deployed off the northern California coast in July and August 1994. The measured radiometric temperatures showed a few Kelvin azimuth modulations in all Stokes parameters with respect to the wind direction. The wind directional signals observed in the 37 GHz channel were similar to those in the 19 GHz channel. This indicates that the wind direction signals in sea surface brightness temperatures have a weak frequency dependence in the range of 19 to 37 GHz. The harmonic coefficients of the wind direction signals were derived from experimental data versus incidence angle. It was found that the first harmonic coefficients, which are caused by the up and downwind asymmetric surface features, had a small increasing trend with the incidence angle. In contrast, the second harmonic coefficients, caused by the up and crosswind asymmetry, showed significant variations in T_v and U data, with a sign change when the incidence angle increased from 45° to 65°. Besides the first three Stokes parameters, the fourth Stokes parameter, V, which had never been measured for sea surfaces before, was measured using our 19-GHz channel. The Stokes parameter V has an odd symmetry just like that of the third Stokes parameter U, but with a smaller wind direction signal than that of U. Theoretical interpretation based on two-scale scattering models was performed to interpret the experimental data. The results are consistent with the assumption of a power-law spectrum for sea surfaces, and indicate that the angular surface spectrum is nearly constant for the part of capillary waves interacting with 19 to 37 GHz electromagnetic waves. In summary, the sea surface features created by the near surface winds are anisotropic in azimuth direction and modulate all Stokes parameters of sea surface microwave brightness temperatures by as large as a few Kelvin in the range of incidence angles from 45° to 65° applicable to spaceborne observations.

1 Introduction

There has be an increasing interest in the application of passive microwave radiometers for ocean wind remote sensing. The near surface ocean wind, generating the momentum flux affecting ocean circulation and mixing, is the key driving force in air-sea interaction processes. Global mapping of near surface ocean winds is crucial for many oceanographic and atmospheric studies. Previous applications of passive microwave radiometers were limited to wind speed measurements based on the sensitivity of thermal emission to surface roughness created by wind forcing. Examples of such radiometers include the Scanning Multichannel Microwave Radiometer (SMMR) flown on NIMBUS-7 and SEASAT and the Special Sensor Microwave/ Imager (S SM/I) deployed on the Defense Meteorological Satellite Program (DMSP) missions [1].

However, recent experimental observations [2, 3, 4, 5] indicated that ocean microwave thermal radiation could vary over azimuthal angles relative to the wind direction by a few Kelvin. The aircraft radiometer experiments conducted by the Russian scientists at the Space Research Institute measured the sea surface brightness temperatures at near normal incidence angles [2, 4]. They found a few Kelvin wind direction signal in the brightness temperatures. Unfortunately, those measurements did not cover the range of incidence angles traditionally used by spaceborne microwave radiometers (incidence angles of 48° to 60°) for large swath coverage. In contrast, SSM/I has measured the brightness temperatures at an incidence angle of 53°. Wentz's SSM/I model function [3] indicated that T_h and T_v at both 19 and 37 GHz could vary with the wind direction by a few Kelvin.

Besides vertical and horizontal polarization measurements made by conventional radiometers, the results collected at near normal incidence by Dzura et al. [4] and the theoretical analysis based on a polarimetric Bragg scattering model by Yueh et al. [6] suggested that radiometric brightness temperatures at all polarization states are also sensitive to wind direction. To explore the potential of polarimetric radiometry for spaceborne remote sensing applications, a K-band multi-polarization radiometer (WINDRAD) was built and deployed

on the NASA DC-8 aircraft with circle flights over several ocean buoys to study sea surface radio emissions by Yueh et al. [5] in November 1993. These measurements were the first experimental evidence indicating that the first three Stokes parameters of sea surface emissions are sensitive to ocean wind direction in the incidence angle range of 30° to 50°. The observed azimuthal signatures of Stokes parameters were shown to agree with the predictions of a two-scale surface emission model [7, 8]. The results of these aircraft flights indicate that passive polarimetric radiometry has a strong potential for global ocean wind speed and direction measurements from space.

However, these experimental data are not yet adequate to design a spaceborne sensor for ocean wind sensing. The key parameters of a spaceborne radiometer system include the frequencies, incidence angle, and radiometric sensitivity. Wentz's SSM/I geophysical model function [3] was limited to the 53° incidence and was for only two polarizations T_v and T_h. Hence, Wentz's SSM/I model function does not allow a tradeoff study of incidence angle and polarization selection. For the cases of the data collected in November 1993 by the Jet Propulsion Laboratory's (JPL) WIN DRAD, the results were three Stokes parameter measurements from 30° to 50° incidence angles. However, they were insufficient to define a geophysical model function due to the limited atmospheric and oceanic conditions encountered. In addition, the 1993 JPL data were limited to one frequency only, thus providing no information about how the signals change with frequency.

To obtain a better understanding of the frequency dependence, a Ka-band (37 GHz) polarimetric radiometer was built and integrated with the K-band (19 GHz) radiometer used in the 1993 WINDRAD experiments. The dual-frequency system was flown in July and August, 1994 over ocean buoys to obtain a more extensive measurement with varying incidence angle, The results are reported in this paper.

Section 2 reviews the polarimetric radiometry theory for sea surfaces and Section 3 describes the dual-frequency polarimetric radiometer system. Section 4 describes the flight experiments and the measured Stokes parameter data. Theoretical interpretation based on

the Bragg scattering model is given in Section 5 and a summary is in Section 6.

2 Microwave Polarimetric Radiometry

The electromagnetic waves emitted from natural media due to random thermal motion of electric charges are in general partially polarized. To fully characterize the polarization state of partially polarized thermal radiation, four parameters I, Q, U, and V were introduced by Sir George Stokes [11]. Because conventional radiometers for earth remote sensing measure T_v and T_h, an alternate representation is to use a modified form of Stokes vector with four parameters, T_v, T_h, U, and V,

$$I_s = \begin{bmatrix} T_v \\ T_h \\ U \\ V \end{bmatrix} = c \begin{bmatrix} < |E_v|^2 > \\ < |E_h|^2 > \\ 2Re < E_v E_h^* > \\ 2Im < E_v E_h^* > \end{bmatrix} \quad (1)$$

T_v and T_h are the brightness temperatures of vertical and horizontal polarizations, while U and V characterize the correlation between these two orthogonal polarizations. Note that $I(=T_v + T_h)$ represents the total radiated energy and $Q(=T_v - T_h)$ the polarization balance. Eq. (1) defines the Stokes parameters in terms of the horizontally and vertically polarized components of electric fields (E_h and E_v). The polarization vectors are related to the direction of propagation and are illustrated in Figure 1. The angular brackets denote the ensemble average of the argument, and c is a proportional constant relating the brightness temperature to the electric energy density [14].

For wind-generated sea surfaces, the surface spectrum is expected to be symmetric with respect to the wind direction (ϕ_w). In other words, the surfaces are statistically inflection symmetric with respect to ϕ_w [10]. Let the azimuthal observation angle of radiometer look direction be denoted by ϕ_r and the relative azimuth angle by $\phi = \phi_w - \phi_r$. Yueh et al. [10] derived from Maxwell's equations using reflection symmetry that T_v and T_h are even functions of ϕ and U and V are odd functions. A typical form of geophysical model functions, relating the brightness temperatures to the geophysical surface parameters, expresses the Stokes parameters in the Fourier series of the relative azimuth angle ϕ. Hence, expanded to

the second harmonic of ϕ,

$$T_v \simeq T_{v0} + T_{v1}\cos\phi + T_{v2}\cos 2\phi \quad (2)$$

$$T_h \simeq T_{h0} + T_{h1}\cos\phi + T_{h2}\cos 2\phi \quad (3)$$

$$U \simeq U_1 \sin\phi + U_2 \sin 2\phi \quad (4)$$

$$V \simeq V_1 \sin\phi + V_2 \sin 2\phi \quad (5)$$

The coefficients of first harmonics account for the up/downwind asymmetric surface features, while those of second harmonics for the up/crosswind asymmetry. All coefficients are functions of near surface wind speed and other sea surface parameters.

A typical approach for Stokes parameter measurements is to carry out the power measurements at vertical and horizontal polarizations and four other polarizations, including 450-linear (E_p), –450-linear (Em), left-hand-circular (E_{lc}), and right-hand-circular (E_{rc}). Specifically, the following identities are used for measuring the third and fourth Stokes parameters:

$$2Re(E_h E_v^*) = 23,1^2 - |E_m|^2 \quad (6)$$

$$2Im(E_h E_v^*) = E_{lc}|^2 - |E_{rc}|^2 \quad (7)$$

where

$$E_p = \frac{E_h + E_v}{\sqrt{2}} \quad (8)$$

$$E_m = \frac{E_h - E_v}{\sqrt{2}} \quad (9)$$

$$E_{lc} = \frac{E_h + iE_v}{\sqrt{2}} \quad (10)$$

$$E_{rc} = \frac{E_h - iE_v}{\sqrt{2}} \quad (11)$$

Recently, it has been demonstrated that all polarization measurements can be carried out using a single antenna and a microwave switch network to coherently combine the vertically and horizontally polarized electric fields [5] To detect E_p and E_m polarization components

requires the coherent sum -an d difference of vertical and horizontal polarization field components. A microwave "Magic-Tee" was used to perform the necessary coherent operation over a 500 MHz bandwidth at 19 GHz [5] and more than 1 GHz bandwidth for the new 37 GHz radiometer. A 90-degree phase-shifter added in the path of vertical polarization channel leading from the antenna to the Magic-Tee allowed the conversion of E_p into E_{lc} and E_m into E_{rc}. By denoting the brightness temperature measurements at these four polarizations as T_p, T_m, Tic, and T_{rc}, U and V can be derived from these four brightness measurements:

$$U = T_p - T_m \tag{12}$$

$$V = T_{lc} - T_{rc} \tag{13}$$

Hence, complex correlations of E_v and E_h can be obtained by using power measurements.

3 Polarimetric Radiometer

A dual-frequency polarimetric radiometer system operating at 19 GHz (K band) and 37 GHz (Ka band) based on the measurement principle described in the above section have been built, installed and used on the NASA DC-8 for ocean wind measurements. This dual-frequency system was an upgrade of the 19 GHz polarimetric radiometer used in the first WINDRAD experiment in November 1993 [5], which was found to be stable and easy for polarimetric calibration. A block diagram of the 19-GHz radiometer is shown in Figure 2, and Table 1 gives the characteristics of both radiometers. The new 37-GHz radiometer is similar to the 19-GHz radiometer, except that there is no 90-degree phase shifter in the 37-GHz radiometer. In the radiometers, a waveguide network is used to switch between the vertical and horizontal polarization channels from the scalar conical antenna horn. The waveguide network also combines the vertically and horizontally polarized signals in a "Magic Tee" to give T_p and T_m. This network was calibrated and adjusted using a HP8510 network analyzer to provide equal losses and path lengths from the antenna to the Magic Tee.

Following the waveguide network, a conventional Dicke switched Tuned Radio Frequency (TRF) radiometer is used to measure the signal power. The detected signals are digitized

using a 12-bit A/D converter and the two radiometers are controlled by a 486 personal computer. The synchronous detection is done by the computer at a 125 Hz switch rate to eliminate gain variations. A noise diode was used to measure the system noise and for temperature calibration and was calibrated with ambient and liquid Nitrogen thermal loads placed in front of the feedhorn.

During the flight measurements, the two radiometers are repeatedly switched between the four polarizations to obtain simultaneous measurements of all polarizations at both frequencies. Because the computer commanded both radiometers for polarization switching simultaneously, both radiometers performed power detection and integration at the same time and held the data in their own sample/hold circuit. This enables simultaneous dual-frequency radiometer measurements. These data are combined with the DC-8 aircraft data including time, aircraft heading, roll, pitch and altitude for later processing. In addition, a real time display of the brightness temperatures versus time is provided to monitor system performance and direct the measurement sequence. Because relatively long integration times are available in the aircraft measurements, a design tradeoff was made to perform sequential polarization switching using the microwave waveguide network. In a spaceborne system, where integration times will be much shorter, a design performing simultaneous detection of all polarizations will be required to achieve more sensitivity.

4 Aircraft Flight Experiments

In July and August 1994, a set of aircraft flights were carried out with the dual-frequency polarimetric radiometer system, which was mounted on the NASA DC-8. Circle flights were performed over the National Data Buoy Center (NDBC) moored buoys deployed off the northern California coast, which provided ocean wind speed and direction measurements. The K- and Ka-band antenna horns were fixed mounted on the DC-8 windows at an angle of 80 degrees from nadir. To measure the data at 45°, 55”, and 65° incidence angles, the DC-8 was banked at 35°, 25°, and 15°, respectively, At each bank angle, DC-8 performed circle

flights, allowing the radiometers to acquire data from all azimuth angles with respect to the surface wind direction. The data have been corrected for the small changes in the aircraft bank angles during the circles using the measurements from wing- wagging flights with the aircraft roll angle quickly varied within ±40°. Aircraft altitude for the circle flights at 25 and 35 degree bank angles was about 27K feet and was about 31K feet for the 15 degree bank. The flight altitude was chosen so that the. location of antenna footprint would be close to the center of the circles, while DC-8 performing circle flights. This ensured that the data were collected over nearly the same area, hence reducing the uncertainty due to potential spatial surface variations.

Figures 3 to 5 illustrate a set of Stokes parameter measurements versus azimuth angles at the nominal incidence angles of 45°, 55°, and 65°, the 37 GHz T_v and T_h data were offset so that they would be near the values of the 19 GHz data for ease of visual comparison. There was a clear sky over the buoy, and the wind was 9 m/s measured by the buoy at 5 meter height, which can be translated into 10 m/s at 20 m elevation based on [9]. There were a few Kelvin wind direction signals in all Stokes parameters, and the wind direction signatures at the incidence angles of 45° and 55° agree well with the data collected in the first WINDRAD experiment [5]: T_v data peaked at the upwind direction, while T_h reached a minimum; U data displayed an odd symmetry, whereas T_v and T_h data had even symmetry. However, the T_v data obtained at 65° incidence angle had a small dip at the upwind direction, unlike the 45° and 55° incidence data. The dip at the upwind direction means that the second harmonic coefficient of T_v is negative at this angle, while those of 45° and 55° incidence angles are positive.

The K- and Ka-band data plotted in Figures 3 to 5 can be used to evaluate the frequency sensitivity of the wind direction signals. It was noted that the azimuth modulations of the data acquired at these two frequencies almost overlap with each other, suggesting that the wind direction signals in all Stokes parameters have a weak frequency dependence in the frequency range of 19 to 37 GHz. This was observed in all data collected throughout the

flight experiments. This could be due to the nature of sea surfaces, which are known to have a wavenumber spectrum closely following a power law, and are thus nearly self-similar at various scales like a fractal surface. Hence, although 19 and 37 GHz thermal emissions interact with different parts of the spectrum according to Bragg scattering, the length scales of surface dominating the scattering normalized by the electromagnetic wavelength would appear similar at these two frequencies. A more quantitative discussion is given in Section 5. This weak frequency dependence implies that 19 and 37 GHz radiometers would provide similar accuracies for the wind direction measurement under clear sky condition. We do, however, expect that 19 GHz channel would be less sensitive to atmospheric effects than 37 GHz channel, while 37 GHz spaceborne radiometer typically would give a better spatial resolution than 19 GHz radiometers for the same antenna size.

Immediately following the set of circle flights, which acquired the first three Stokes parameter data illustrated in Figures 3 to 5, another set was repeated to acquire the fourth Stokes parameter data, which had never been measured before for ocean remote sensing. This was designed to find out whether there were any wind direction signals in the fourth Stokes parameter, V, of sea surface emission. The phase shifter in the K-band radiometer was set to 90 degrees, enabling simultaneous T_v, T_h, and V measurements. (Note that our 37 GHz channel did not have the 90-degree phase shifter, and hence could not measure the fourth Stokes parameter.) Figure 6 illustrates the wind direction signals in V. It was found that the azimuthal modulation of V is smaller than that of U measured in the first set of circle flights. The fourth Stokes parameter also has an odd symmetry just like the third Stokes parameter. This data set represents the first empirical measurements of the fourth Stokes parameter of sea surface brightness temperatures.

To illustrate the dependence of wind direction signal on incidence angle, we extracted the harmonic coefficients from the data collected over these two consecutive sets of flights over the same buoy. The harmonic coefficients defined in Eqs. (2) to (5) were extracted using the minimum mean square error criterion.

Figure 7 illustrates the first and second harmonic coefficients as functions of incidence angle. In general, all first harmonic coefficients showed a small increasing trend, meaning that up/downwind asymmetric surface features have a slightly more significant effect on the surface emission at a larger incidence angle. When compared with Wentz's SSM/I geophysical model function [3], his T_v model value is in excellent agreement with the data measured from the first set of circle flights, albeit with a 0.5 Kelvin difference with the data from the second set of flights. Additionally, Wentz's SSM/I model indicated a larger first harmonic coefficient in T_h data than our K-band data, but a very similar magnitude with our Ka-band data. At this moment, it is not clear what caused the discrepancy at K-band. A potential factor is the geographical difference: Wentz's SSM/I model was derived from data collected over the globe, representing a mean value of all possible environmental parameters, including sea surface temperature, salinity, and significant wave height, while our data were collected over the northern Pacific ocean off the California coast, and hence, the observed signature might be pertinent to this region and the time of data collection.

Unlike the first harmonic coefficients, the second harmonic coefficients of T_v and U show significant variations over incidence angles, while those of T_h and V showed little variation. T_v data were positive at 45° incidence angle, cross over zero around 55° incidence angle, and became negative at 65° incidence angle. These characteristics are very similar to the wind speed sensitivity of T_v versus incidence angles. T_v is known to have positive wind speed sensitivity and negative sensitivity at small and large incidence angles, respectively, and is insensitive to wind speed change at about 55° incidence angle [12, 13]. Similar variation was seen in U data, though the data crosses zero at an angle near 63 degrees for 19 GHz data and 59 degrees for 37 GHz data. Unlike T_v and U data, the T_h and V curves did not change sign and had no significant variation over 45° to 65° incidence angles. It should be noted that the magnitude of V is in general smaller than that of U except at large incidence angles.

Comparing the data between the first and second sets of circle flights indicated that the second harmonic coefficients were very repeatable, while the first harmonic data had larger

variations. Note that it appeared that the first harmonic data collected at 65° incidence angle were more repeatable than at smaller incidence angles. This could be a result of the fact that the 65° data were collected in closer temporal proximity. The first set of circle flights started at 45° and ended at 65° incidence, and immediately after that the second set of circle flights continued three more circles of 65° incidence and stepped down to 45° incidence. Hence, the data collected at 65° incidence angles were more temporally and spatially coincident, while the data collected at 45° incidence angle were separated by about an hour between these two sets of flights and the radiometer footprints were further apart. Further experiments are required to find the statistical uncertainty of harmonic coefficients.

There was another set of circle flights carried out at a lower wind speed than that of the data described above. The buoy wind data was 7 m/sat 5 m elevation, which corresponds to 8 m/sat 19.5 m elevation [9]. Figure 8 illustrates the harmonic coefficients versus wind speed. In general, the magnitudes of harmonic coefficients arc increasing functions of wind speed as expected. Note that the data measured at 65° incidence angle appeared to have a larger wind speed sensitivity than the data collected at smaller incidence angles. In particular, the first harmonic coefficients of 65° incidence data increase more than by a factor of 2 from 7 to 9 m/s wind. As mentioned previously, the first harmonic coefficients of T_h data were significantly lower than that of Wentz's SSM/I model. Other than that, the agreement between our data collected at 55° incidence and Wentz's SSM/I model [3] is reasonably good. However, the results presented here should be considered preliminary and treated with great caution, because of the uncertainty associated with the ground truth measurements. The wind speed quoted here was the wind speed averaged over 10 minutes before the end of each hour, and was expected to be different from the wind speed at the time of circle flights. In fact, it can be noticed that T_v and T_h data illustrated in Figs. 3 and 4 have a slow upward drifting trend, which could be due to the change of wind speed in time. Additionally, the buoy wind speed was a point measurement, unlike the radiometer received the signals from an area illuminated by the antenna beam. Hence, it is expected that there could be more

than ±1 m/s uncertainty in specifying the wind speed, This means that the slopes of the curves in Fig. 8 have to be considered preliminary. Comparison of the data shown here with measurements at lower wind speeds is required to conclude the trend of wind speed dependence.

5 Theoretical Interpretation

The dual-frequency measurements presented above indicate that the wind direction signals in the Stokes parameters are not a strong function of frequency ranging from 19 to 37 GHz. It is shown below that this experimental observation agrees with the theoretical Bragg scattering model for sea surfaces with a power-law wavenumber spectrum.

As shown in [6], the Stokes parameters are related to the scattering coefficients of sea surfaces by a polarimetric Kirchhoff's law:

$$I_s = T_s' \begin{pmatrix} 1 \\ 1 \\ 0 \\ 0 \end{pmatrix} - I_r \tag{14}$$

where I_r is a vector representing the surface effectivity, and T_s' is the surface temperature. Based on the second order solution of scattering from slightly perturbed rough surfaces [6], I_r can be separated into I_{rc} and I_{ri}, respectively, the coherent and incoherent surface reflectivities:

$$I_r = I_{rc} + I_{ri} \tag{15}$$

I_{ri} is the integral of incoherent polarimetric bistatic scattering coefficients $\gamma^i_{\alpha\beta\mu\nu}$ over all incidence angles in the upper hemisphere:

$$I_{ri} = \int_0^{\pi/2} \sin\theta_i d\theta_i \int_0^{2\pi} d\phi_i \frac{\cos\theta_i}{4\pi\cos\theta} \begin{bmatrix} \gamma^i_{vvvv}(\theta,\phi;\theta_i,\phi_i) + \gamma^i_{vhvh}(\theta,\phi;\theta_i,\phi_i) \\ \gamma^i_{hhhh}(\theta,\phi;\theta_i,\phi_i) + \gamma^i_{hvhv}(\theta,\phi;\theta_i,\phi_i) \\ 2Re(\gamma^i_{vhhh}(\theta,\phi;\theta_i,\phi_i) + \gamma^i_{vvhv}(\theta,\phi;\theta_i,\phi_i)) \\ 2Im(\gamma^i_{vhhh}(\theta,\phi;\theta_i,\phi_i) + \gamma^i_{vvhv}(\theta,\phi;\theta_i,\phi_i)) \end{bmatrix} \tag{16}$$

The bistatic scattering coefficients are related to the wavenumber spectrum W of sea surfaces

by

$$\gamma^{i}_{\alpha\beta\mu\nu}(\theta,\phi;\theta_i,\phi_i) = \frac{4\pi k_0^4 \cos^2\theta\, F_{\alpha\beta\mu\nu}(\theta,\phi;\theta_i,\phi_i) W(k_\rho\cos\phi - k_{\rho i}\cos\phi_i, k_\rho\sin\phi - k_{\rho i}\sin\phi_i)}{\cos\theta_i} \tag{17}$$

Here, θ and ϕ signify the zenith and azimuth angles of the propagation direction of scattering waves, and θ_i and ϕ_i the zenith and azimuth angles of the propagation direction of the incident wave. $k_\rho = k_0 \sin\theta$ and $k_{\rho i} = k_0 \sin\theta_i$ are the magnitudes of the scattered and incident wave vectors projected on the horizontal plane. k. is the free-space electromagnetic wavenumber. The expressions of scattering coefficients, $F_{\alpha\beta\mu\nu}$, are given in Appendix A.

The coherent reflectivity I_{rc} with the second order scattered field considered can be expressed as [6]

$$I_{rc} = \begin{vmatrix} \left|R^{(0)}_{vv}\right|^2 + 2Re(R^{(0)}_{vv}R^{(2)*}_{vv}) \\ \left|R^{(0)}_{hh}\right|^2 + 2Re(R^{(0)}_{hh}R^{(2)*}_{hh}) \\ 2Re(R^{(2)}_{vh}R^{(0)*}_{hh} + R^{(0)}_{vv}R^{(2)*}_{hv}) \\ 2Im(R^{(2)}_{vh}R^{(0)*}_{hh} + R^{(0)}_{vv}R^{(2)*}_{hv}) \end{vmatrix} \tag{18}$$

Here, $R^{(0)}_{vv}$ and $R^{(0)}_{hh}$ are the Fresnel reflection coefficients for vertically and horizontally polarized incident fields, respectively, and $R^{(2)}_{\alpha\beta}$ with α and β being v or h is the correction of specular reflection coefficients caused by the small surface perturbation [6]:

$$R^{(2)}_{\alpha\beta} = \int_0^{2\pi}\int_0^{\infty} k_0^2 W(k_\rho\cos\phi - k_{\rho i}\cos\phi_i, k_\rho\sin\phi - k_{\rho i}\sin\phi_i) g^{(2)}_{\alpha\beta} k_\rho dk_\rho d\phi \tag{19}$$

where $k_{\rho i} = k_0 \sin O_i$ is the transverse component of the incident wavenumber, and the expression of $g^{(2)}_{\alpha\beta}$ is given in Appendix B.

Based on the Bragg scattering model of sea surfaces, capillary waves are the dominant scattering sources for centimeter- wavelength elect romagnet ic waves, The wind-generated capillary waves have been known to have a power law wavenumber spectrum. In the following analysis, it is assumed that the part of wavenumber spectrum, which interacts strongly with 19 to 37 GHz electromagnetic waves, has the following form:

$$W(k_x, k_y) = \frac{B}{k^4}(1 + b\cos 2\chi) \tag{20}$$

where k_x and k_y are the wavenumbers along and perpendicular to the surface wind direction, respectively, and k and χ are the wavenumber and azimuthal angle of the wave vector in polar coordinate. The parameter b, characterizing the degree of up and crosswind asymmetry, is in general a function of k, but can be assumed to be a constant for the range of wavenumber considered. This assumption is shown to be supported by our aircraft radiometer observations.

Note that the sea surface spectrum does not rise like $1/k^4$ at low wavenumbers, but instead will roll off to zero at low k. To more rigorously treat the scattering from sea surfaces with a continuous wavenumber spectrum, t we-scale surface scattering models have been developed by many researchers, such as that given in [15, 7, 8]. In two-scale surface scattering models, the surface spectrum has been separated into two parts with a cutoff wavenumber k_d. The waves with $k > k_d$ arc the small-scale waves, which cause the Bragg scattering, while the large-scale waves with $k < k_d$ cause a change in local incidence and scattering geometry. The scattering effects of large-scale waves have been treated by geometric optics in two-scale scattering models. Because the geometric optics scattering mechanism is independent of frequency and the slopes of large-scale sea surfaces are small enough that the effects of averaging over slope distribution are not significant for surface reflectivity, it is only necessary to focus on the effects of Bragg scattering on the frequency sensitivity of sea surface emissivity.

To investigate the effects of Bragg scattering on the frequency sensitivity of I_{ri} and $R^{(2)}_{\alpha\beta}$, which are expressed as the integrals over the wavenumber spectrum weighted by scattering coefficients, two issues need to be addressed. One is whether the integrands of the integrals are sensitive to frequency, and the other is whether the integration limits of the integrals implied by the wavenumber cutoff $k > k_d$ are sensitive to frequency.

Under the assumption of the power-law wavenumber spectrum given by Eq. (20), it is shown by Eq. (48) in Appendix C that the wavenumber spectrum W in the integrals for I_{ri} and $R^{(2)}_{\alpha\beta}$ is proportional to $1/k_0^4$. This term will cancel out the k_0^4 term in Eq. (17). Likewise,

substituting Eq. (48) into Eq. (19) and changing the integration variable to $\xi = k_\rho/k_0$ yield

$$R^{(2)}_{\alpha\beta} = \int\int \frac{B}{2\pi} \frac{1+b\frac{\xi^2\cos 2\phi+\xi_i^2\cos 2\phi_i-2\xi\xi_i\cos(\phi+\phi_i)}{\xi^2+\xi_i^2-2\xi\xi_i\cos(\phi-\phi_i)}}{\left[\xi^2+\xi_i^2-2\xi\xi_i\cos(\phi-\phi_i)\right]^2} g^{(2)}_{\alpha\beta}\xi d\xi d\phi \tag{21}$$

where $\xi_i = \sin\theta_i$. The result is that the integrands in both integrals are not explicit functions of k_0 or electromagnetic frequency.

Although $\gamma^i_{\alpha\beta\mu\nu}$ and the integrand for $R^{(2)}_{\alpha\beta}$ appear to be independent of k_0, it should be noticed that the scattering coefficients $F_{\alpha\beta\mu\nu}$ and $g^{(2)}_{\alpha\beta}$ are functions of sea surface dielectric constant ϵ, which may vary significantly over microwave frequencies, Nevertheless, since ϵ is much larger than one at microwave frequencies, the scattering coefficients have been shown to be insensitive to ϵ in Appendices A and B. (Note that $\epsilon >> \xi$ has been used to approximate $g^{(2)}_{\alpha\beta}$. This is justified because as shown in Eq. (21) the integrand decays faster than $1/\xi^3$ at large ξ, indicating that the integrand has a non-negligible contribution only when ξ is of the order of 1 or less.) The above discussion leads to the conclusion that the integrands in the integrals for I_{ri} and $R^{(2)}_{\alpha\beta}$ are insensitive to the frequency.

Next, it is shown that the integration limit implied by the cutoff wavenumber of the capillary waves contributing to the Bragg scattering is insensitive to frequency. This is made apparent by normalizing both sides of $k > k_d$ by k_0, resulting in

$$\sqrt{\xi^2+\xi_i^2-2\xi\xi_i\cos(\phi-\phi_i)} > \xi_d \tag{22}$$

in terms of the normalized variables $\xi = k_\rho/k_0, \xi_i = \sin\theta_i$, and $\xi_d = k_d/k_0$. For the integral for I_{ri}, ξ reduces to $\sin\theta$. In two-scale scattering modelling of sea surfaces, the cutoff wavenumber k_d is adjusted according to the frequency of incident electromagnetic waves. Because the electromagnetic waves interact strongly only with the portion of capillary waves with wavenumbers close to k_o, and because the surfaces with $1/k^4$ spectrum are self-similar at changing length scales, the cutoff wavenumber k_d of the short waves should be proportional to k_0 so that the short waves after normalized by the electromagnetic wavelength will appear the same. This means that the ratio k_d/k_0 is *close* to a constant. Consequently, the integration limit implied by the wavenumber cutoff is insensitive to frequency.

Because the azimuthal dependence of I_r is caused by the variations of I_{ri} and $R^{(2)}_{\alpha\beta}$ over azimuth angles, and because these two terms are shown to be weak functions of electromagnetic frequencies with the assumption of a power-law wavenumber spectrum, theoretical wind direction signals based on the Bragg scattering model for capillary waves with a power law spectrum will be a weak function of frequency. To verify the above discussion, theoretical simulation based on a two-scale polarimetric sea surface emission model [7, 8] was performed at 19 and 37 GHz. The two-scale model splits the spectrum into the short and long wave spectra, with the effects of long and short waves modelled by the geometric optics and Bragg scattering theories. Hydrodynamic modulation was also introduced to enhance the magnitude of short waves riding on the downwind side of long waves, resulting in the up and downwind asymmetry in the theoretical data. The results were illustrated in Figures 9 and 10 for 55° and 65° incidence angles. It can be seen that there is no significant difference between the azimuthal variations of theoretical Stokes parameters at these two frequencies. Comparison has also been made for 45° incidence angle. The agreement is better than those shown in Figures 9 and 10, and hence the comparison is not presented. In conclusion, the results showed that the wind direction signals in all measured Stokes parameters agreed reasonably well with the predictions of Bragg scattering mechanism. Nevertheless, the difference between the theory and data suggests that either the second-order perturbation solution used in the two-scale model is not accurate enough for sea surface scattering, or there are other contributing scattering mechanisms, like foams and breaking waves, which need to be considered.

6 Summary

A set of successful dual-frequency airborne radiometer flights were carried out to investigate the wind direction sensitivity of the Stokes parameters of microwave emissions from sea surfaces. The aircraft was banked at three different angles to acquire the data in the incidence angle range of 45° to 65°. There were as large as a few Kelvin signals observed in all Stokes

parameters. Preliminary assessment of the frequency sensitivity, incidence angle dependence, and wind speed dependence was performed. It was found that the wind direction signals have a broad frequency spectrum from 19 to 37 GHz. 'l'he up and downwind asymmetry of sea surface brightness had a small increasing trend versus incidence angle, while the up and crosswind asymmetry may have a dramatic variation with incidence angle. The observed magnitudes of azimuthal wind direction signals in T_v and T_h, though weak compared with the direction-independent terms (T_{v0} and T_{h0}), are easily measurable with present microwave radiometers. In addition, the third and fourth Stokes parameters, U and V, which have an odd symmetry with respect to the wind direction, hence free of the zero harmonic term, are also measurable with a single antenna plus microwave switch network design, The results indicate that spaceborne passive microwave radiometers have a strong potential for ocean wind remote sensing.

However, further flight experiments are required to gather data at low wind (3 to 5 m/s) and high wind (above 15 m/s) to allow a more complete evaluation of the wind speed dependence of wind direction signals in sea surface brightness temperatures. The effects of other environmental variables, including air and sea surface temperatures (SST), significant wave height, and atmospheric water content, also need to be investigated. 'I'he permittivity of sea surfaces is a function of SST, meaning that a change of SST will lead to a change of surface emissivity and the magnitudes of all harmonic coefficients. In addition, the air and sea surface temperature difference affects the stability of surfaces and the onset of breaking waves. The whitecaps caused by breaking waves are known to be a significant rni crowave radiation source. The large scale waves and swells would affect the local incidence angle and the friction velocity or wind stress of sea surfaces, which directly influences the magnitude of short-scale wind waves and therefore the modulation of microwave emission from sea surfaces. Atmospheric liquid water and water vapor in addition to other constituents, will attenuate the microwave emission from the surface, and the atmospheric downwelling reflection from the surface has a negative effect on the wind direction signals in the surface emission. The effects of these

variables need to be quantified to understand the limitation of passive microwave radiometry and to develop techniques applicable to reduce these effects for ocean wind remote sensing.

7 Acknowledgment

‘l’his work was performed under contract with the National Aeronautics and Space Administration at the Jet Propulsion Laboratory, California Institute of ‘1’ethnology. The authors would like to thank David Orozco, David Huynh, and Paul Batelaan, of JPL for their technical help, and John Reller, Christi Scofield, Chris Miller and the DC-8 aircraft flight crew of the NASA Ames Research Center for assistance in aircraft flight planning and experiments.

A First-order scattering coefficients

The coefficients for the incoherent bistatic scattering coefficients due to the first-order scattered fields arc defined as:

$$F_{\alpha\beta\mu\nu}(\theta,\phi;\theta_i,\phi_i) = g^{(1)}_{\alpha\beta}(\theta,\phi;\theta_i,\phi_i)g^{(1)*}_{\mu\nu}(\theta,\phi;\theta_i,\phi_i) \tag{23}$$

with

$$g^{(1)}_{hh}(\theta,\ \phi;\ \theta_i,\ \phi_i) = \frac{2\cos\theta_i(\epsilon-1)}{(\cos\theta+\sqrt{\epsilon-\sin^2\theta})(\cos\theta_i+\sqrt{\epsilon-\sin^2\theta_i})}\cos(\phi-\phi_i) \tag{24}$$

$$g^{(1)}_{hv}(\theta,\ \phi;\ \theta_i,\ \phi_i) = \frac{2\cos\theta_i(\epsilon-1)\sqrt{\epsilon-\sin^2\theta_i}}{(\cos\theta+\sqrt{\epsilon-\sin^2\theta})(\epsilon\cos\theta_i+\sqrt{\epsilon-\sin^2\theta_i})}\sin(\phi-\phi_i) \tag{25}$$

$$g^{(1)}_{vh}(\theta,\ \phi;\ \theta_i,\ \phi_i) = \frac{2\cos\theta_i(\epsilon-1)\sqrt{\epsilon-\sin^2\theta}}{(\epsilon\cos\theta+\sqrt{\epsilon-\sin^2\theta})(\cos\theta_i+\sqrt{\epsilon-\sin^2\theta_i})}\sin(\phi-\phi_i) \tag{26}$$

$$g^{(1)}_{vv}(\theta,\phi;\ \theta_i,\phi_i) = \frac{2\cos\theta_i(\epsilon-1)\left[\epsilon\sin\theta\sin\theta_i-\sqrt{\epsilon-\sin^2\theta}\sqrt{\epsilon-\sin^2\theta_i}\cos(\phi-\phi_i)\right]}{(\epsilon\cos\theta+\sqrt{\epsilon-\sin^2\theta})(\cos\theta_i+\sqrt{\epsilon-\sin^2\theta_i})} \tag{27}$$

If $\epsilon \gg 1$,

$$g^{(1)}_{hh}(\theta,\phi;\theta_i,\phi_i) \approx 2\cos\theta_i\cos(\phi-\phi_i) \tag{28}$$

$$g^{(1)}_{hv}(\theta,\phi;\theta_i,\phi_i) \approx \frac{2\cos\theta_i}{\cos\theta_i+\frac{\sqrt{\epsilon}}{\epsilon}}\sin(\phi-\phi_i) \tag{29}$$

$$g^{(1)}_{vh}(\theta,\phi;\theta_i,\phi_i) \approx \frac{2\cos\theta_i}{\cos\theta+\frac{\sqrt{\epsilon}}{\epsilon}}\sin(\phi-\phi_i) \tag{30}$$

$$g^{(1)}_{vv}(\theta,\phi;\theta_i,\phi_i) \approx \frac{2\cos\theta_i}{(\cos\theta+\frac{\sqrt{\epsilon}}{\epsilon})(\cos\theta_i+\frac{\sqrt{\epsilon}}{\epsilon})}\left[\sin\theta\sin\theta_i-\cos(\phi-\phi_i)\right] \tag{31}$$

Hence, the above coefficients are relatively insensitive to the surface permittivity, except when θ and θ_i become comparable to or greater than the Brewster angle, which is about 80° for sea surfaces.

B Second-order scattering coefficients

The correction terms of the coherent reflection coefficients due to second-order scattered fields are given as follows:

$$g_{hh}^{(2)} = \frac{2\cos\theta_i(\epsilon-1)}{(\cos\theta_i+\sqrt{\epsilon-\sin^2\theta_i})^2}\left\{\sqrt{\epsilon-\sin^2\theta_i}\right.$$
$$-\frac{(\epsilon-1)}{(\xi^2+\sqrt{\epsilon-\xi^2}\sqrt{1-\xi^2})(\sqrt{\epsilon-\xi^2}+\sqrt{1-\xi^2})}$$
$$\left.\left[\sqrt{\epsilon-\xi^2}\sqrt{1-\xi^2}+\xi^2\cos^2(\phi-\phi_i)\right]\right\} \quad (32)$$

$$g_{vh}^{(2)} = \frac{2\cos\theta_i(\epsilon-1)\sin(\phi-\phi_i)}{(\cos\theta_i+\sqrt{\epsilon-\sin^2\theta_i})(\epsilon\cos\theta_i+\sqrt{\epsilon-\sin^2\theta_i})(\xi^2+\sqrt{\epsilon-\xi^2}\sqrt{1-\xi^2})}$$
$$\left[\epsilon\xi\sin\theta_i-\frac{(\epsilon-1)\xi^2\sqrt{\epsilon-\sin^2\theta_i}\cos(\phi-\phi_i)}{(\sqrt{\epsilon-\xi^2}+\sqrt{1-\xi^2})}\right] \quad (33)$$

$$g_{hv}^{(2)} = -g_{vh}^{(2)} \quad (34)$$

$$g_{vv}^{(2)} = \frac{2\cos\theta_i(1-\epsilon)\epsilon}{(\epsilon\cos\theta_i+\sqrt{\epsilon-\sin^2\theta_i})^2}\left\{\frac{(\epsilon-1)\xi^2\sin^2\theta_i}{(\xi^2+\sqrt{\epsilon-\xi^2}\sqrt{1-\xi^2})(\sqrt{\epsilon-\xi^2}+\sqrt{1-\xi^2})}\right.$$
$$+\sqrt{\epsilon-\sin^2\theta_i}\left[1-\frac{2\xi\sin\theta_i\cos(\phi-\phi_i)}{\xi^2+\sqrt{\epsilon-\xi^2}\sqrt{1-\xi^2}}\right]$$
$$\left.-\frac{(\epsilon-\sin^2\theta_i)(\epsilon-1)}{\epsilon(\sqrt{\epsilon-\xi^2}+\sqrt{1-\xi^2})}\left[1-\frac{\xi^2\cos^2(\phi-\phi_i)}{\xi^2+\sqrt{\epsilon-\xi^2}\sqrt{1-\xi^2}}\right]\right\} \quad (35)$$

where

$$\xi = \frac{k_\rho}{k_0} \quad (36)$$

If $\epsilon \gg 1$ and $\epsilon \gg \xi$, then

$$g_{hh}^{(2)} \approx \frac{2\cos\theta_i\xi^2}{\frac{\xi^2}{\sqrt{\epsilon}}+\sqrt{1-\xi^2}}\sin^2(\phi-\phi_i) \quad (37)$$

$$g_{vh}^{(2)} \approx \frac{2\cos\theta_i\xi^2}{(\cos\theta_i+\frac{1}{\sqrt{\epsilon}})(\frac{\xi^2}{\sqrt{\epsilon}}+\sqrt{1-\xi^2})}\sin(\phi-\phi_i)\left[\xi\sin\theta_i-\xi^2\cos(\phi-\phi_i)\right] \quad (38)$$

$$g_{vv}^{(2)} \approx \frac{-2\cos\theta_i\left[\xi^2\sin^2\theta_i-2\xi\sin\theta_i\cos(\phi-\phi_i)+\xi^2\cos^2(\phi-\phi_i)\right]}{(\cos\theta_i+\frac{1}{\sqrt{\epsilon}})^2(\frac{\xi^2}{\sqrt{\epsilon}}+\sqrt{1-\xi^2})} \quad (39)$$

C Wavenumber spectrum

The wavenumber spectrum of sea surfaces can be represented by the following general expression:

$$W(k_x, k_y) = \frac{1}{2\pi k} S(k)\Phi(k, \chi) \tag{40}$$

where $k = \sqrt{k_x^2 + k_y^2}$ and

$$\cos \chi = \frac{k_x}{k} \tag{41}$$

$$\sin \chi = \frac{k_y}{k} \tag{42}$$

S accounts for the magnitude of spectrum as a function of wavenumber, and Φ for the angular variation of the spectrum caused by winds. A typical form of Φ is

$$\Phi(k, \chi) = 1 + b(k) \cos 2\chi \tag{43}$$

By using the above equations, it can be shown that

$$W(k_\rho \cos\phi - k_{\rho i}\cos\phi_i, k_\rho \sin\phi - k_{\rho i}\sin\phi_i) = \frac{S(k)}{2\pi k}\left[1 + b(k)\cos 2\chi\right] \tag{44}$$

where

$$k = \sqrt{k_\rho^2 + k_{\rho i}^2 - 2k_\rho k_{\rho i}\cos(\phi - \phi_i)} \tag{45}$$

$$\cos 2\chi = \frac{k_\rho^2 \cos 2\phi + k_{\rho i}^2 \cos 2\phi_i - 2k_\rho k_{\rho i}\cos(\phi + \phi_i)}{k^2} \tag{46}$$

If the high wavenumber portion of the spectrum is assumed to be

$$S(k) = \frac{B}{k^3} \tag{47}$$

then

$$W(k_\rho \cos\phi - k_{\rho i}\cos\phi_i, k_\rho \sin\phi - k_{\rho i}\sin\phi_i) = \frac{B}{2\pi k_0^4} \frac{1 + b\frac{\xi^2\cos 2\phi + \xi_i^2 \cos 2\phi_i - 2\xi\xi_i\cos(\phi+\phi_i)}{\xi^2 + \xi_i^2 - 2\xi\xi_i\cos(\phi-\phi_i)}}{\left[\xi^2 + \xi_i^2 - 2\xi\xi_i\cos(\phi - \phi_i)\right]^2} \tag{48}$$

where $\xi = k_\rho/k_0$ and $\xi_i = \sin\theta_i$.

References

[1] Hollinger, J. P., J. L. Peirce, and G. A. Poe, "SSM/I Instrument Evaluation," *IEEE Trans. Geosci. Remote Sensing,* Vol. 28, No. 5, 781-790, Sept, 1990.

[2] Etkin, V. S., M.D. Raev, M.G. Bulatov, Yu.A. Militsky, A.V. Smirnov, V.Yu. Raizer, Yu.A. Trokhimovsky, V.G. Irisov, A.V. Kuzmin, K.Ts. Litovchenko, E.A. Bespalova, E.I. Skvortsov, M.N. Pospelov, and A.I. Smirnov, *Radiohydrophysical Aerospace Research of Ocean,* Report IP-1749, Academy of Sciences, Space Research Institute, Moscow, USSR, 1991.

[3] Wentz, F. J., "Measurement of oceanic wind vector using satellite microwave radiometers," *IEEE Tmns. Geosci. Remote* Sensing, Vol. 30, No. 5, 960-972, Sep., 1992.

[4] Dzura, M. S., V. S. Etkin, A. S. Khrupin, M. N. Pospelov, and M. D. Raev, "Radiometers-Polarimeters: principles of design and applications for sea surface microwave emission polarimetry," Proceedings of International Geoscience and Remote Sensing Symposium, Houston, 1992.

[5] Yueh, S. H., W. J. Wilson, F. K. Li, W. Il. Ricketts, and S. V. Nghiem, "Polarimetric measurements of sea surface brightness temperatures using an aircraft K-band radiometer," accepted for publication in *IEEE Trans.* Geoscience *and Remote Sensing,* August 1994.

[6] Yueh, S. H., R. Kwok, F. K. Li, S. V. Nghiem, W. J. Wilson, and J. A. Kong, "Polarimetric passive remote sensing of ocean wind vector," *Radio Science*, 799-814, July-August, 1994.

[7] Yueh, S. H., R. Kwok, F. K. Li, S. V. Nghiem, W. J. Wilson, and J. A. Kong, "Polarimetric passive remote sensing of wind-generated sea surfaces and ocean wind vectors," Proceedings of Ocean symposium, Vol. 1, 31-36, Victoria, British Columbia, Canada, October 1993.

[8] Yueh, S. H., S. V. Nghiem, and R. Kwok, "Comparison of a polarimetric scattering and emission model with ocean backscatter and brightness temperatures, " Proceedings of International Geoscience and Remote Sensing symposium, Pasadena, 1994.

[9] Large, W. G., and S. Pond, "Open ocean momentum flux measurements in moderate to strong winds," *J. Phys. Oceanogr.*, 11, 324-336, 1981.

[10] Yueh, S. H., R. Kwok, and S. V. Nghiem, "Polarimetric scattering and emission properties of targets with reflection symmetry," *Radio* Science, Vol. 29, No. 6, 1409-1420, November-December, 1994.

[11] Kraus, John D., Radio Astronomy, 2nd. cd., 1986, Cygnus-Quasar Books, Powell, Ohio.

[12] Hollinger, J. P., "Passive microwave measurements of sea surface roughness," *IEEE Tmns. Geosci. Electronics,* Vol. GE-9, No. 3, 165-169, July 1971.

[13] Sasaki, Yasunori, Ichio Asanuma, Kei Muneyama, Gen'Ichi Naito, and Tsutomu Suzuki, "The dependence of sea-surface microwave emission on wind speed, frequency, incidence angle, and polarization over the frequency range from 1 to 40 GHz," *IEEE* Trans. *Geosci. and Remote Sensing,* Vol. GE-25, No. 2, 138-146, March, 1987.

[14] Yueh, S. H., and R,. Kwok, "Electromagnetic fluctuations for anisotropic media and the generalized Kirchhoff's law," Radio Science, Volume 28, No. 4, pp. 471-480, July-August 1993.

[15] DoneIan, M. A., and W. J. Pierson, "Radar scattering and equilibrium ranges in wind-generated waves with applications to scatterometry," *J. Geophys. Res.*, Vol. 92, No. c5, 4971-5029, May 15, 1987.

List of Tables

Parameter	Value	
Frequency (GHz)	19.35	37
Antenna Beamwidth (degree)	3.9	6.3
Antenna Sidelobes (dB)	-23	-33
Polarization	V, H, 45(R*),-45(L*)	V, H, 45°, -45°
Dicke Switch Rate (Hz)	125	125
Radiometer Bandwidth (MHz)	500	1200
Noise Diode Temperature (K)	103	78
System Noise Temp. (K)	550	620
Total System Noise Temp. for Scene** (K)	803	898
RMS noise for 1.6 sec integration** (K)	0.06	0.04
Absolute calibration (K)	<4	< 4
Aircraft Altitude*** (Kft)	27, 31	27, 31
Nominal Aircraft Ground Track Speed (Knot/h)	400	400

Table 1: WINDRAD key parameters. *: Phase shifter set at 90 degrees phase shift. **: Assume 150 K background for 19 GHz and 200 K background for 37 GHz. ***: 27 Kft for 45 and 55 degree incidence and 31 Kft for 65° incidence

List of Figures

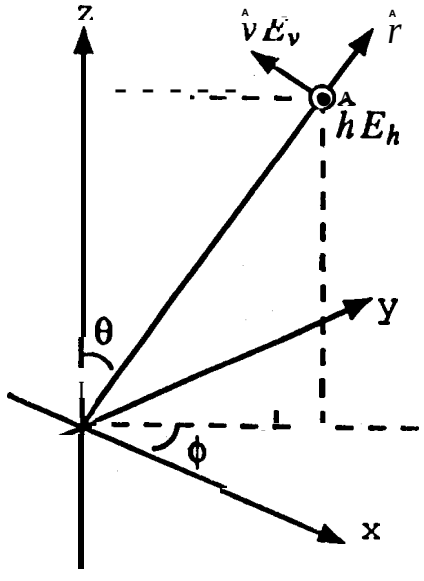

Figure 1

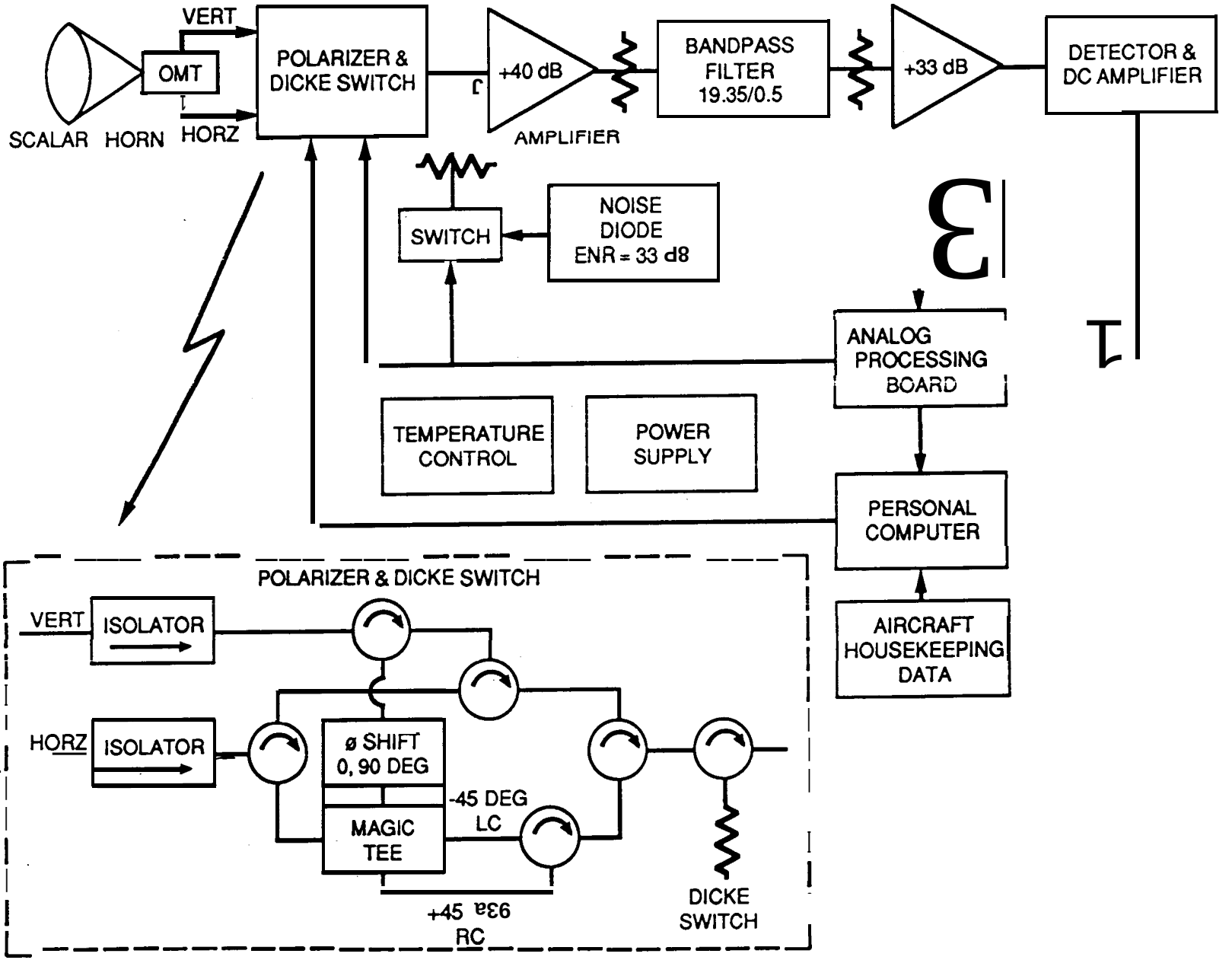
VERT
OMT
HORZ
SCALAR HORN
POLARIZER & DICKE SWITCH
+40 dB
AMPLIFIER
BANDPASS FILTER 19.35/0.5
+33 dB
DETECTOR & DC AMPLIFIER
SWITCH
NOISE DIODE ENR = 33 dB
ANALOG PROCESSING BOARD
TEMPERATURE CONTROL
POWER SUPPLY
PERSONAL COMPUTER
AIRCRAFT HOUSEKEEPING DATA
POLARIZER & DICKE SWITCH
VERT
ISOLATOR
HORZ
ISOLATOR
ø SHIFT 0, 90 DEG
-45 DEG LC
MAGIC TEE
+45 RC
DICKE SWITCH

JPL WINDRAD'94 07062247

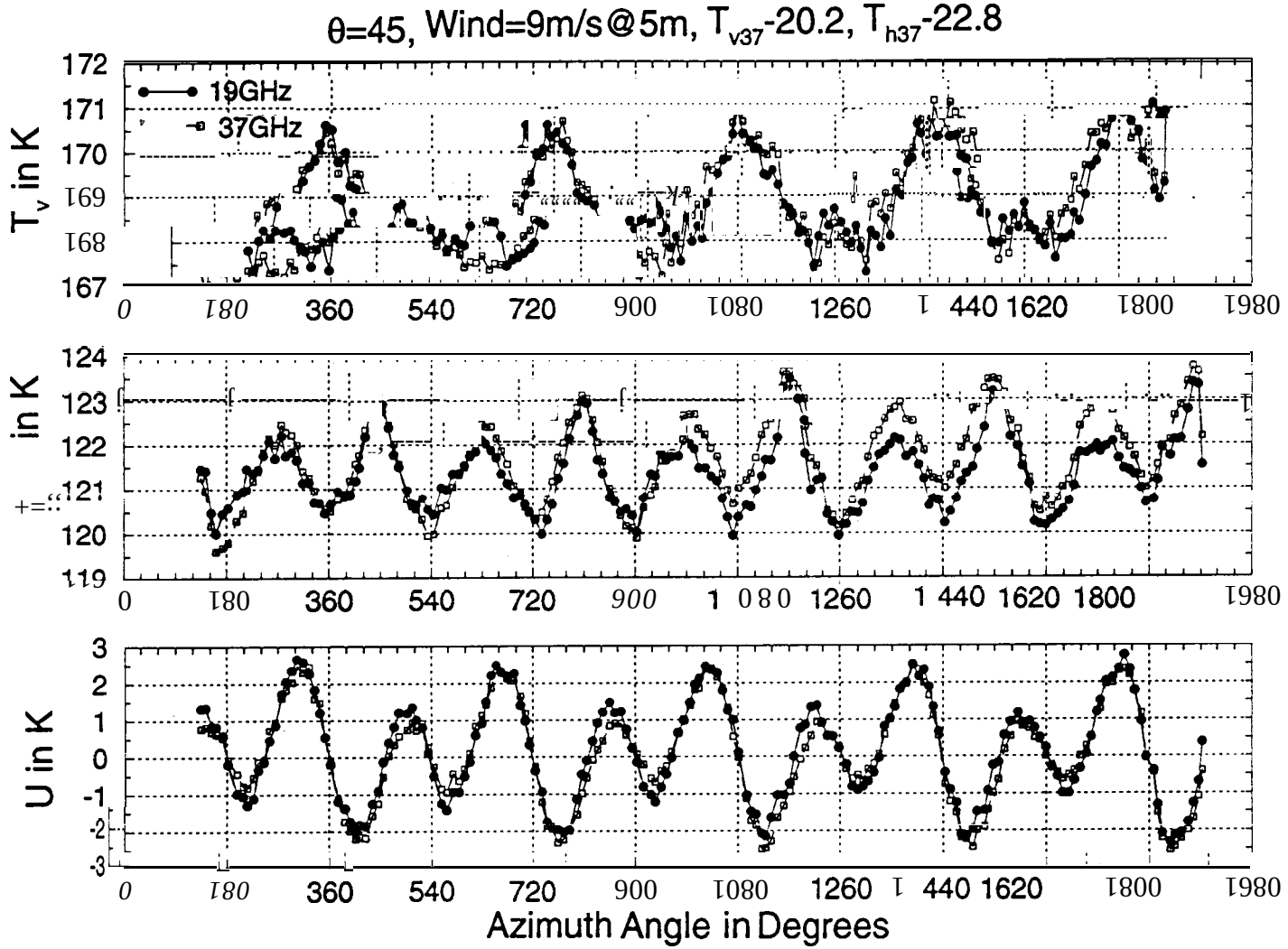

Fig. 3

JPL WINDRAD'94 07062308

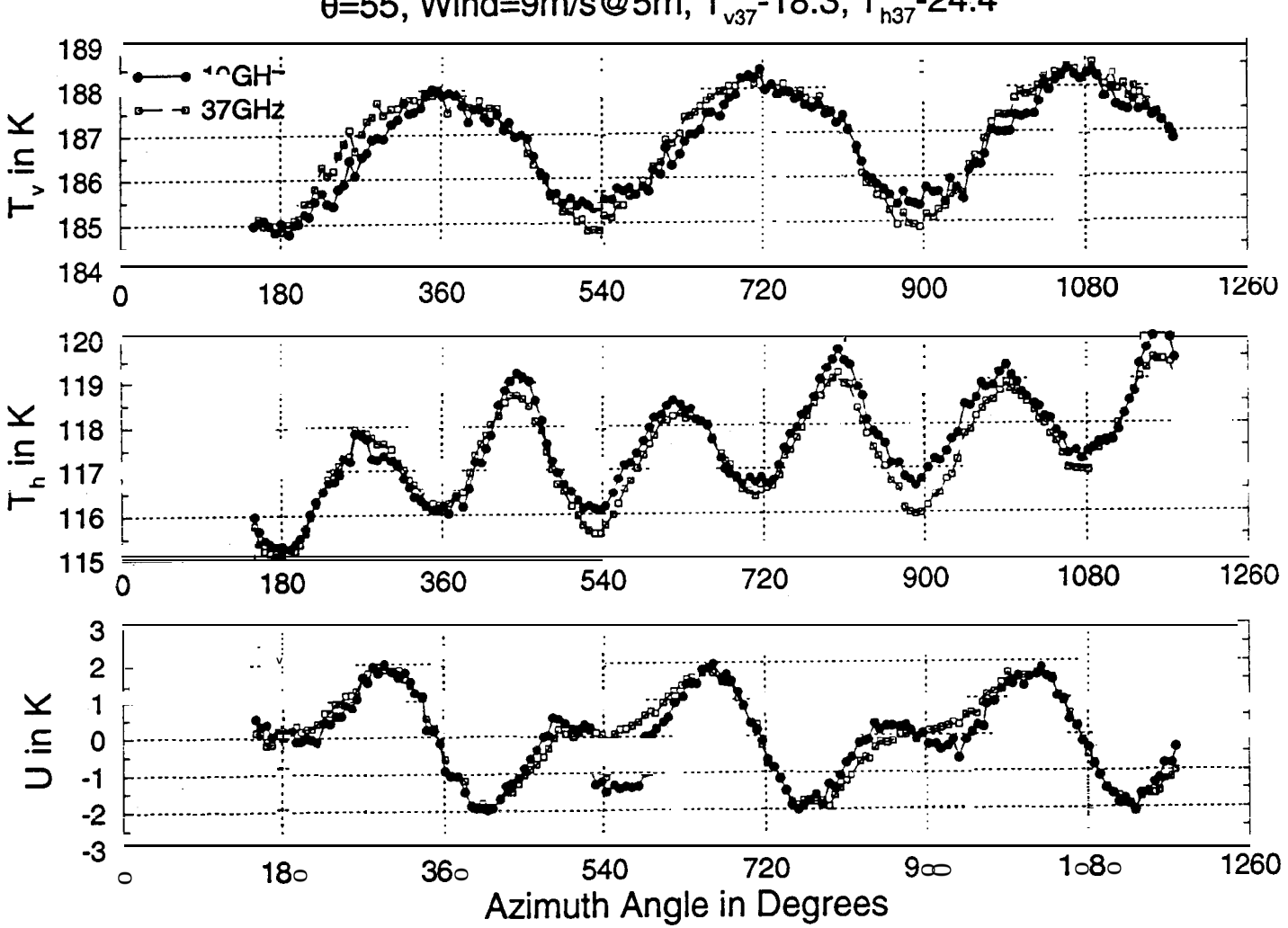

Fig 4

JPL WINDRAD'94 07062328

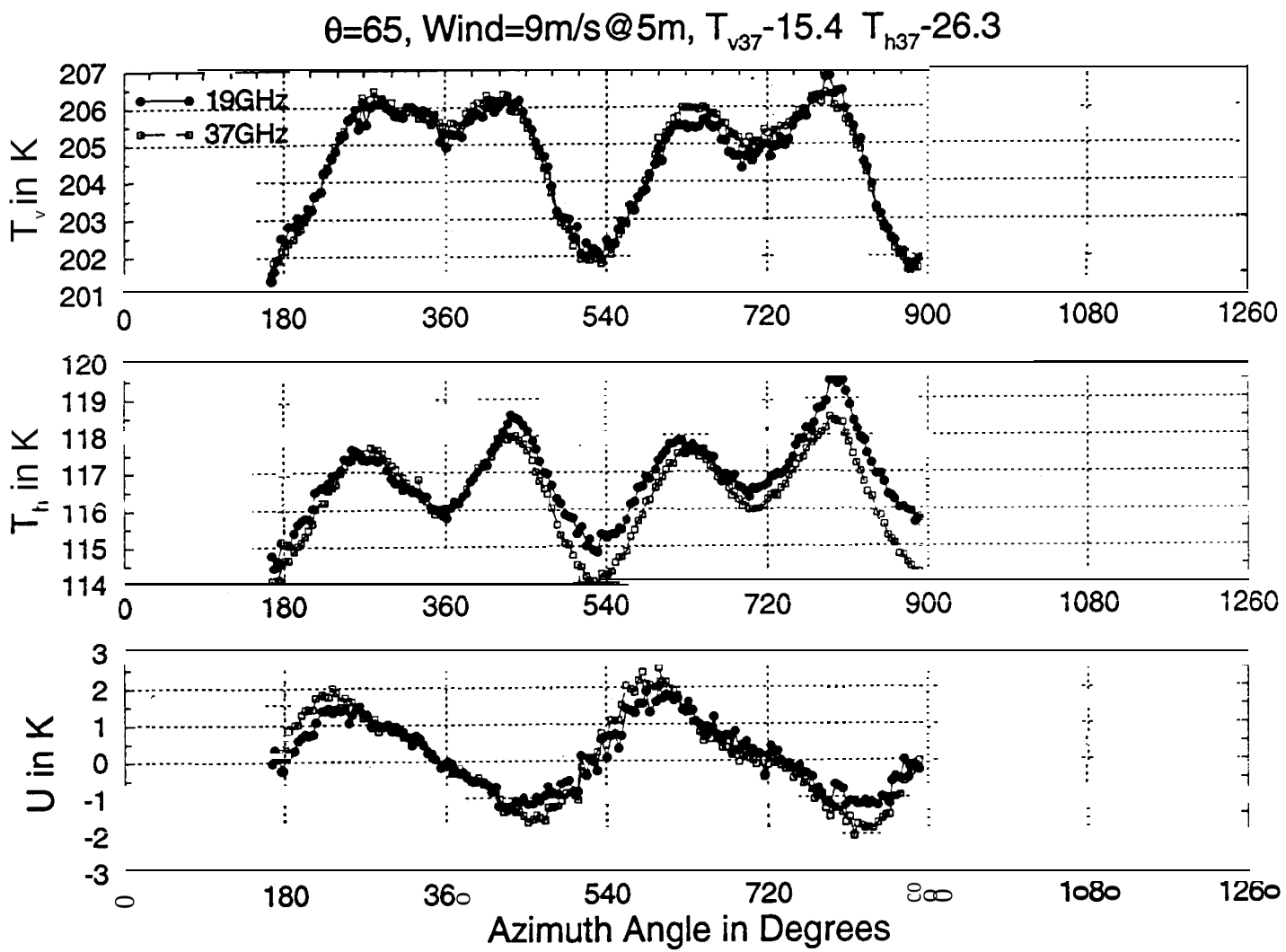

Fig. 5

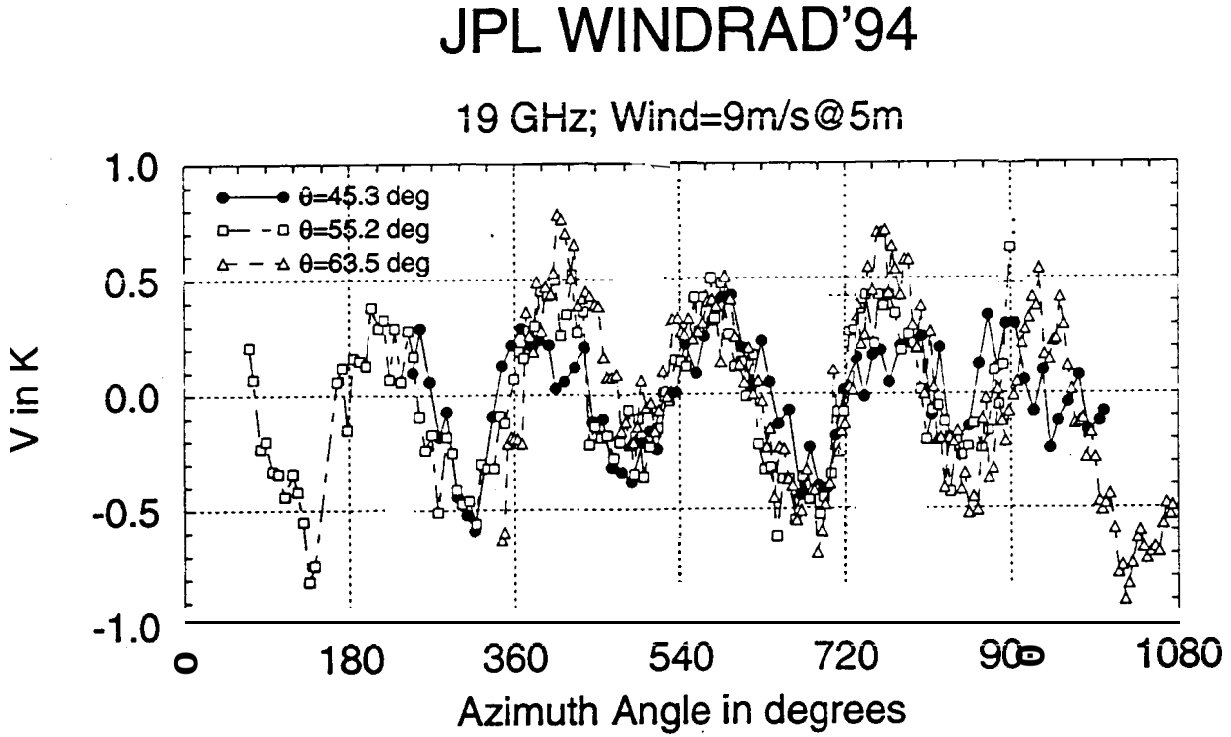
JPL WINDRAD'94
19 GHz; Wind=9m/s@5m
θ=45.3 deg
θ=55.2 deg
θ=63.5 deg
V in K
1.0
0.5
0.0
-0.5
-1.0
0
180
360
540
720
900
1080
Azimuth Angle in degrees

Fig. 6

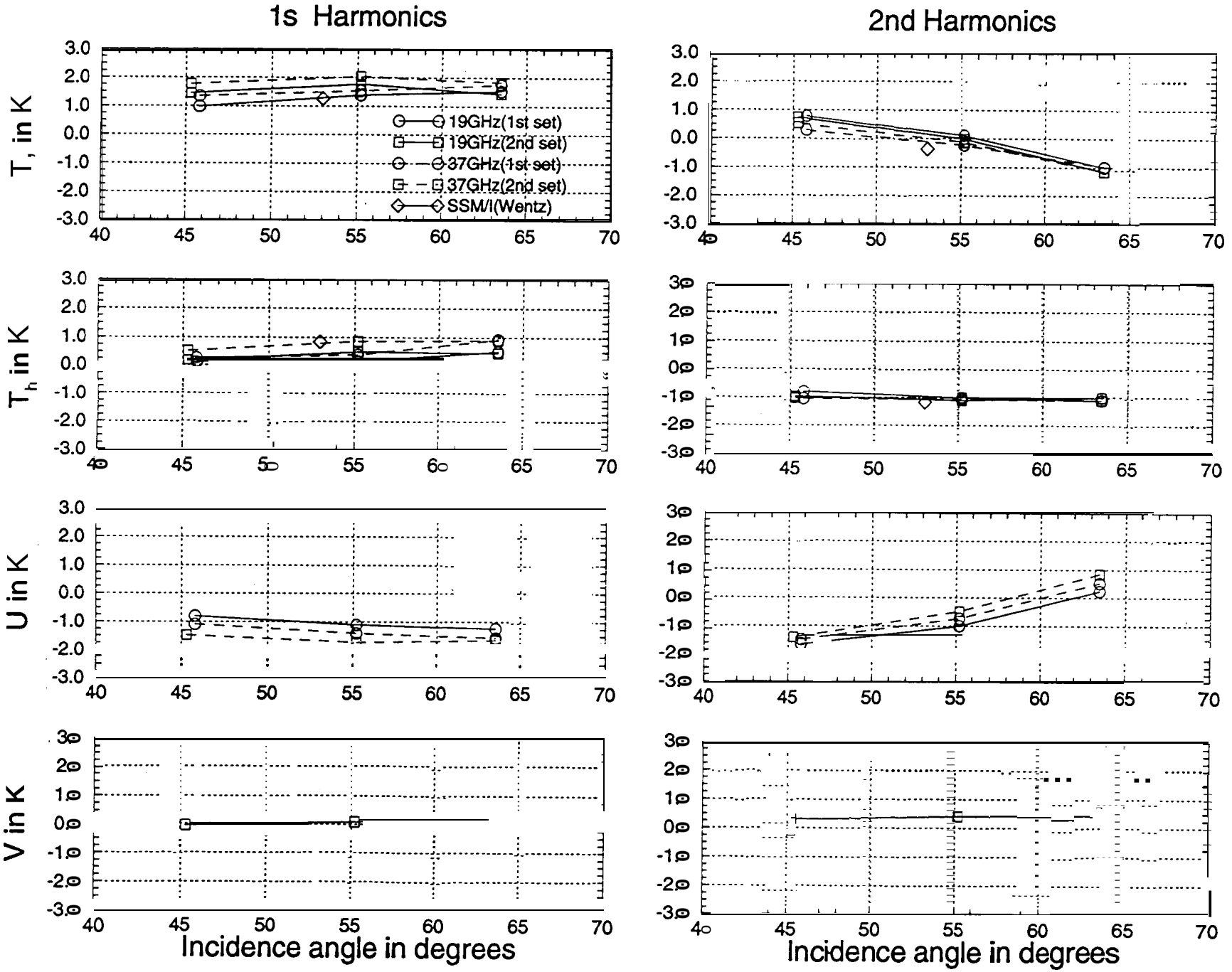
1s Harmonics
2nd Harmonics
T, in K
T_h in K
U in K
V in K
19GHz(1st set)
19GHz(2nd set)
37GHz(1st set)
37GHz(2nd set)
SSM/I(Wentz)
Incidence angle in degrees
Incidence angle in degrees

Fig. 7

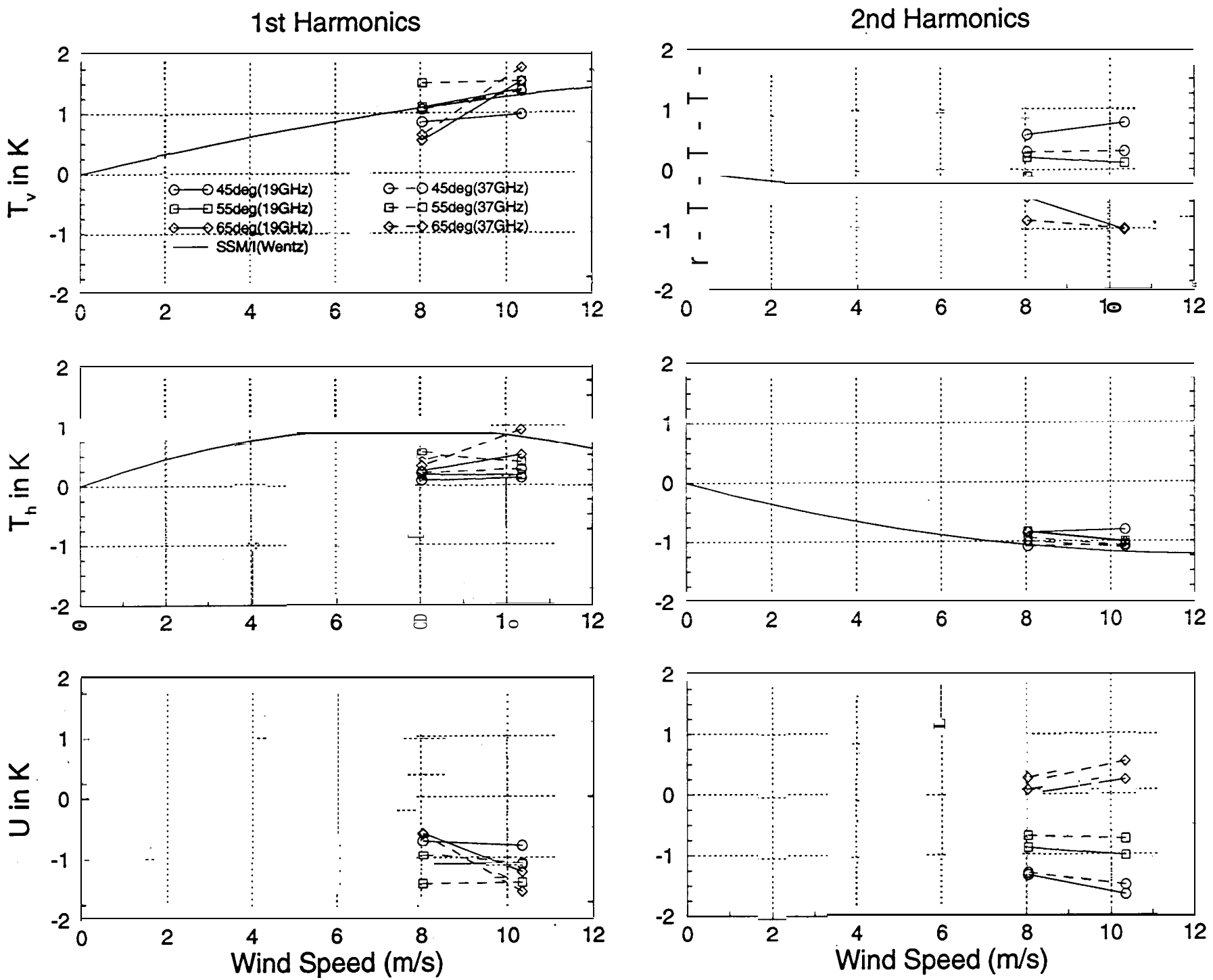
1st Harmonics
2nd Harmonics
T_v in K
T_h in K
U in K
45deg(19GHz)
55deg(19GHz)
65deg(19GHz)
SSM/I(Wentz)
45deg(37GHz)
55deg(37GHz)
65deg(37GHz)
Wind Speed (m/s)
Wind Speed (m/s)

Fig 8

JPL W NDRAD'94 DATA VS. THEORY

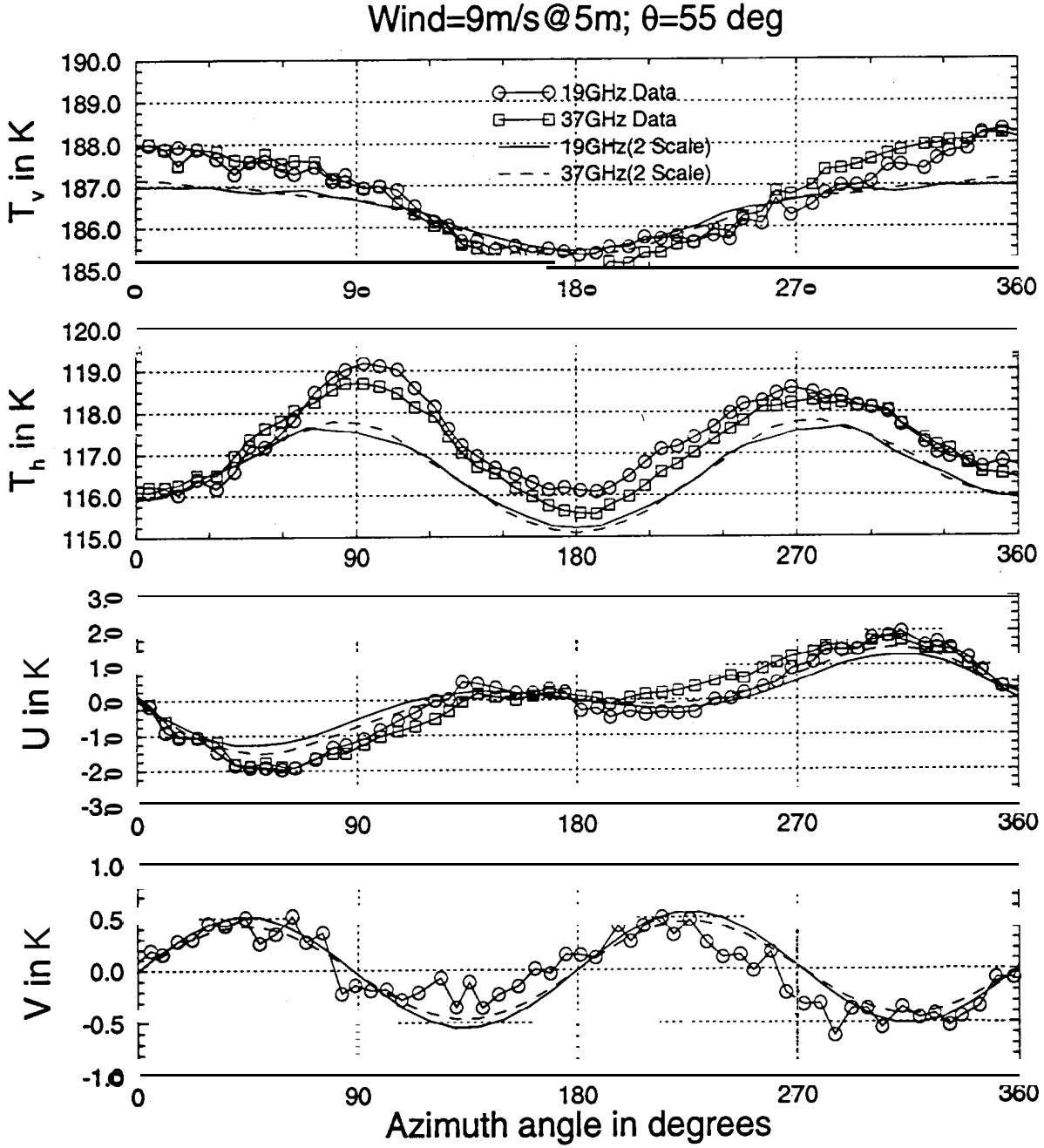

Fig. 9

JPL WINDRAD'94 DATA VS. THEORY

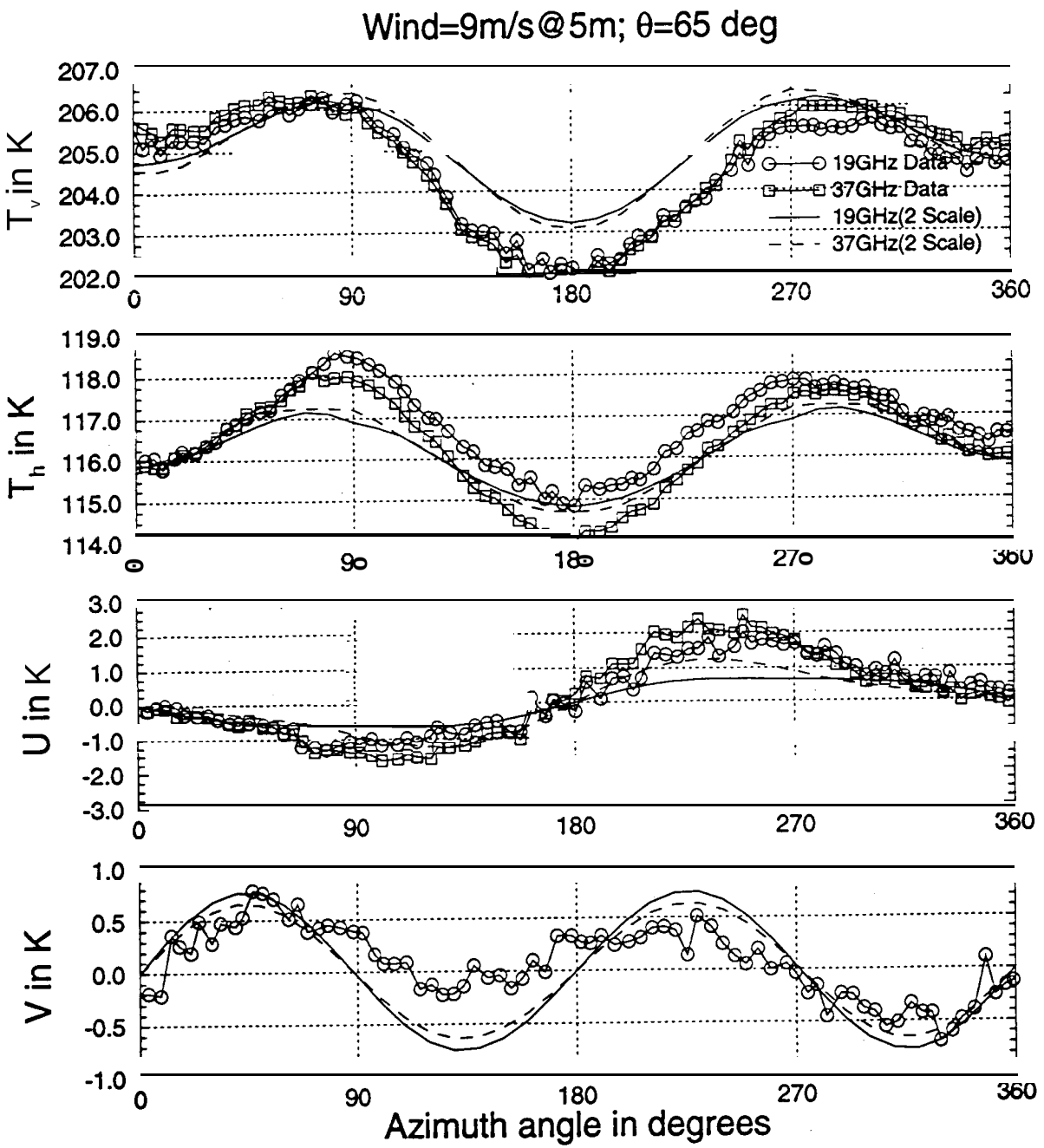

Fig 10